JOURNAL OF GEOPHYSICAL RESEARCH, VOL. 106, NO. D10, PAGES 10,313–10,323, MAY 27, 2001

Retrieval of molecular nitrogen and molecular oxygen densities in the upper mesosphere and lower thermosphere using ground-based lidar measurements

M. M. Mwangi, R. J. Sica, and P. S. Argall

Department of Physics and Astronomy, The University of Western Ontario, London, Ontario, Canada

Abstract. Two new techniques have been developed to estimate the densities of N_2, O_2, and O from Rayleigh lidar backscatter photocount profiles and from independent temperature determinations. Both techniques involve solving initial value problems for the N_2, O_2, and O densities. These initial value problems are derived from the lidar equation, the ideal gas law, and the assumption of hydrostatic equilibrium. Their solutions are valid in regions where the Rayleigh lidar backscatter can be fully isolated from other scattering sources, e.g., aerosol scattering and where independent temperature determinations can been made. Estimates of the N_2 and O_2 density profiles in the upper mesosphere and lower thermosphere have been performed on three nights using simultaneous sodium-resonance-fluorescence lidar measurements to independently determine the temperature profile. The available measurements are of insufficient quality to retrieve O density profiles. The resulting N_2 and O_2 density retrievals appear reasonable when compared with previous determinations from sounding rockets and give hope that this method will allow routine ground-based measurements of major constituent density in the middle atmosphere. A detailed error analysis is described which shows that the primary source of random errors is the Rayleigh photocounts, while the most important systematic errors are uncertainties in the N_2 and O_2 Rayleigh backscatter cross sections and in the normalization of the lidar density profiles in the upper stratosphere and lower mesosphere.

1. Introduction

The University of Western Ontario Purple Crow Lidar System can simultaneously obtain measurements of Rayleigh backscatter at a wavelength of 532 nm and sodium-resonance-fluorescence backscatter at wavelengths near 589 nm. For a description of the aforementioned Rayleigh and sodium lidar systems, see *Sica et al.* [1995] and *Argall et al.* [2000] respectively. Argall et al. show temperature measurements in the upper mesosphere and lower thermosphere derived from both the Rayleigh and sodium-resonance-fluorescence backscatter lidars. These independent and simultaneous determinations of temperatures were found to disagree to an extent greater than would be expected solely from experimental uncertainties.

Temperature profiles are derived from Rayleigh backscatter using methods similar to that described by *Hauchecorne and Chanin* [1980]. To devise these methods, it is assumed that the mixing ratio of the major atmospheric constituents is constant with height, with a value typically chosen equal to its sea level value. However, this assumption is not made when temperature profiles are derived from sodium resonance fluorescence backscatter [e.g., *Gibson et al.*, 1979; *Fricke and von Zahn*, 1985; *She et al.*, 1992]. The disagreement found by Argall et al. suggests that the mixing ratio of the major atmospheric constituents is not always equal to its sea level value in the upper mesosphere and lower thermosphere. Neutral composition measurements made by rocket-borne mass spectrometers have observed differences from sea level values [e.g., *Philbrick et al.*, 1973, 1974, 1978; *Trinks et al.*, 1978; *Krankowsky et al.*, 1979; *Offermann et al.*, 1981]. For example, *Offermann et al.* [1981] reported mixing ratios of O_2 to N_2 in the upper mesosphere and lower thermosphere which were smaller than their sea level value by as much as 40%.

It will be shown that the densities of N_2 and O_2 can be derived from sodium-resonance-fluorescence backscatter temperature measurements and Rayleigh backscatter photocount profiles obtained by the Purple Crow Lidar. Measurements of these densities are important for understanding the coupling between the dynamics and the chemistry of the atmosphere in the upper mesosphere and lower thermosphere.

Paper number 2000JD900669.
0148-0227/01/2000JD900699$09.00

2. Initial Value Problem for N_2 and O_2 Densities

2.1. Fundamental Equations

The first equation needed to determine the major constituent densities is a correspondence between lidar photocounts and species density. For altitudes $z > 30$ km the expected received photon count for a Rayleigh lidar system is given by the lidar equation in the form

$$N(z) = \eta T_a^2 \left[\frac{P_L \Delta t}{(hc)/\lambda_L}\right][\bar{\sigma}_R(z) n(z) \Delta z]\left(\frac{A_R}{4\pi z^2}\right) + N_B R_L \Delta t \quad (1)$$

where $N(z)$ is the expected number of Rayleigh and background

photons detected in the range interval $(z-\Delta z/2,\ z+\Delta z/2)$, η is the lidar efficiency, T_a is the one way transmittance of the atmosphere, P_L is the laser power, Δt is the integration time, h is Planck's constant, c is the speed of light, λ_L is the wavelength of the laser, $\bar{\sigma}_R(z)$ is the mean Rayleigh backscatter cross section of the atmosphere, $n(z)$ is the number density of the atmosphere, Δz is the receiver range bin length, A_R is the receiving telescope aperture area, N_B is the expected photon count per range bin per pulse due to background noise and dark counts, and R_L is the laser pulse rate [*Gardner et al.*, 1989]. The altitude z in the lidar equation is measured relative to the observatory. Typically, lidar measurements are presented in height relative to mean sea level (as is the case for the Purple Crow Lidar measurements). In this study, Δt is chosen to be about 5 hours, and Δz is chosen to be 144 m.

Equation (1) can be expressed in the simplified form

$$N_R(z) = \frac{1}{\alpha z^2}\bar{\sigma}_R(z)n(z), \tag{2}$$

where

$$N_R(z) = N(z) - N_B R_L \Delta t, \tag{3}$$

$$\alpha = \frac{4\pi hc}{\eta T_a^2 P_L \Delta t \lambda_L \Delta z A_R} \tag{4}$$

By substituting the appropriate expression for $\bar{\sigma}_R(z)$ into (2), the right-hand side of (2) can be expressed in terms of the number densities $n^i(z)$ and the Rayleigh backscatter cross sections σ_R^i of the individual atmospheric species:

$$N_R(z) = \frac{1}{\alpha z^2}\sum_i \sigma_R^i n^i(z) \tag{5}$$

The convention employed in (5) will be used hereinafter. Wherever the index i is used, it will be assumed that i runs through all atmospheric species unless explicitly stated otherwise.

The value of α can be found using a model atmosphere, since Rayleigh-scatter lidars can only infer relative density profiles. For this study, the MSIS model was used [*Hedin*, 1987]. As described by *Sica et al.* [1995], we normalize the Rayleigh-scatter measurements to the total density of the atmosphere from 45 to 60 km. In this height interval, $\bar{\sigma}_R(z)$ can be taken to equal its sea level value with very little loss of accuracy,

$$\bar{\sigma}_R(z) = \bar{\sigma}_R = 6.002 \times 10^{-32}\ \mathrm{m}^2, \tag{6}$$

for $45\ \mathrm{km} \le z \le 60\ \mathrm{km}$ at a wavelength of 532 nm [*Measures*, 1984]. Let $n_m(z)$ be the number density of the atmosphere at the height z as computed using the MSIS model. Then from (2) and (6), the normalization of the Rayleigh photocounts to density is

$$\alpha = \bar{\sigma}_R \cdot \frac{\int_{45\ \mathrm{km}}^{60\ \mathrm{km}} n_m(z)dz}{\int_{45\ \mathrm{km}}^{60\ \mathrm{km}} z^2 N_R(z)dz} \tag{7}$$

The second equation needed is an equation of state. At all altitudes z of interest, the atmosphere obeys the ideal gas law

$$P(z) = \frac{R}{N_A}T(z)\sum_i n^i(z), \tag{8}$$

where $P(z)$ is the pressure, R is the universal gas constant, N_A is Avagadro's number, and $T(z)$ is the temperature.

The final equation is a relation between the pressure and the gravitational force. On a sufficiently long time scale and a large length scale, the atmosphere can be treated as if it is in hydrostatic equilibrium

$$\frac{dP}{dz}(z) = -\frac{1}{N_A}g(z)\sum_i M^i n^i(z), \tag{9}$$

where $g(z)$ is the acceleration due to gravity, and M^i are the molecular masses of the individual atmospheric species. In practice, to satisfy this assumption, nightly profiles averaged over 4 to 5 hours of measurement are used. To further minimize wave effects, the measurements are coadded to 144 m vertical resolution and smoothed in height with a 3 km low-pass filter. No obvious gravity wave breaking events occurred on the nights chosen for analysis, which could compromise the hydrostatic assumption.

2.2. Derivation of the Initial Value Problem for the N_2 and O_2 Densities

With very little loss of accuracy, the atmosphere in the upper mesosphere and lower thermosphere can be taken to consist only of N_2, O_2, Ar, and O, with N_2 and O_2 being by far the most abundant species. Then, (5), (8), and (9) reduce to

$$N_R(z) = \frac{1}{\alpha z^2}[\sigma_R^{N_2} n^{N_2}(z) + \sigma_R^{O_2} n^{O_2}(z) + \sigma_R^{Ar} n^{Ar}(z) + \sigma_R^{O} n^{O}(z)], \tag{10}$$

$$P(z) = \frac{R}{N_A}T(z)[n^{N_2}(z) + n^{O_2}(z) + n^{Ar}(z) + n^{O}(z)], \tag{11}$$

$$\frac{dP}{dz}(z) = -\frac{1}{N_A}g(z) \times [M^{N_2} n^{N_2}(z) + M^{O_2} n^{O_2}(z) + M^{Ar} n^{Ar}(z) + M^{O} n^{O}(z)] \tag{12}$$

respectively. Multiplying each side of (10) by $\alpha z^2/\sigma_R^{N_2}$ and differentiating each side of the resulting equation with respect to z yields

$$\frac{dn^{N_2}}{dz}(z) + \frac{\sigma_R^{O_2}}{\sigma_R^{N_2}}\frac{dn^{O_2}}{dz}(z) = u(z), \tag{13}$$

where

$$u(z) = \frac{\alpha z}{\sigma_R^{N_2}}\left[z\frac{dN_R}{dz}(z) + 2N_R(z)\right] - \frac{\sigma_R^{Ar}}{\sigma_R^{N_2}}\frac{dn^{Ar}}{dz}(z) - \frac{\sigma_R^{O}}{\sigma_R^{N_2}}\frac{dn^{O}}{dz}(z) \tag{14}$$

Differentiating each side of (11) with respect to z and substituting the resulting expression for $dP(z)/dz$ into the left-hand side of (12) gives

$$\frac{dn^{N_2}}{dz}(z) + \frac{dn^{O_2}}{dz}(z) = v(z), \tag{15}$$

where

$$v(z) = -\frac{1}{T(z)}\sum_i\left[\frac{dT}{dz}(z) + \frac{M^i}{R}g(z)\right]n^i(z) - \frac{dn^{Ar}}{dz}(z) - \frac{dn^{O}}{dz}(z) \quad (16)$$

Solving for $dn^{N_2}(z)/dz$ and $dn^{O_2}(z)/dz$ in equations (13) and (15) yields

$$\frac{dn^{N_2}}{dz}(z) = \frac{u(z) - \sigma_R^{O_2}\,v(z)/\sigma_R^{N_2}}{1 - \sigma_R^{O_2}/\sigma_R^{N_2}}, \quad (17)$$

$$\frac{dn^{O_2}}{dz}(z) = \frac{v(z) - u(z)}{1 - \sigma_R^{O_2}/\sigma_R^{N_2}} \quad (18)$$

An examination of (14) and (16) reveals that the right-hand sides of (17) and (18) depend on the quantities $N_R(z)$, $T(z)$, α, R, M^i, σ_R^i, $g(z)$, and $n^i(z)$. The temperature profile is assumed to be obtained independently of the Rayleigh-scatter measurement. The constant α can be computed using (7), and the quantities R, M^i, σ_R^i, and $g(z)$ are known. Table 1 lists the values of the Rayleigh backscatter cross sections at a wavelength of 532 nm. The only unknowns on the right-hand sides of (17) and (18) are the densities $n^i(z)$. It turns out (as will be discussed later) that the Ar and O densities can be taken from a model with little loss of accuracy for the retrieval of N_2 and O_2 densities.

The density retrievals are valid in regions where the Rayleigh scattering is the dominate scattering mechanism, and an independent determination of temperature exists. Rayleigh scattering is the dominate scattering mechanism at altitudes above about 30 km. For the results that are to follow, the independent temperature profile is derived from narrow-bandwidth sodium resonance fluorescence backscatter measurements, so $T(z)$ and $dT(z)/dz$ are only known at altitudes between approximately 80 and 105 km. At the lowest height of the density retrieval, $z \cong 80$ km, the ratio $n^{O_2}(z)/n^{N_2}(z)$ can be taken from the MSIS model with little loss of accuracy,

$$\frac{n^{O_2}(z_o)}{n^{N_2}(z_o)} = \beta_o \quad (19)$$

where the zero subscript refers to the lowest height of the retrieval. From (10) the Rayleigh photocounts at this height are

$$N_R(z_o) = \frac{1}{\alpha z_o^2}\left[\sigma_R^{N_2}n^{N_2}(z_o) + \sigma_R^{O_2}n^{O_2}(z_o) + \sigma_R^{Ar}n^{Ar}(z_o) + \sigma_R^{O}n^{O}(z_o)\right] \quad (20)$$

Table 1. Rayleigh Backscattering Cross Sections for N_2, O_2, Ar, and O at a Wavelength of 532 nm

Species	Cross Section ($\times 10^{-32}$ m^2)	Reference
N_2	6.21	*Measures* [1984]
O_2	5.22	*Measures* [1984]
Ar	5.80	*Measures* [1984]
O	1.1	*Stergis* [1966]

Solving for $n^{N_2}(z_o)$ and $n^{O_2}(z_o)$ in (19) and (20) gives

$$n^{N_2}(z_o) = \frac{\alpha z_o^2 N_R(z_o) - \sigma_R^{Ar}n^{Ar}(z_o) - \sigma_R^{O}n^{O}(z_o)}{\sigma_R^{N_2} + \sigma_R^{O_2}\beta_o}, \quad (21)$$

$$n^{O_2}(z_o) = \beta_o\, n^{N_2}(z_o) \quad (22)$$

Equations (17)-(18) and (21)-(22) represent an initial value problem that can be solved for $n^{N_2}(z)$ and $n^{O_2}(z)$.

3. Solution of the Initial Value Problem for the N_2 and O_2 Densities

The initial value problem represented by (17)-(18) and (21)-(22) can be expressed as

$$\frac{d\boldsymbol{n}}{dz}(z) = \boldsymbol{f}(\boldsymbol{n}(z), z; \alpha, \sigma_R^i, N_R(z), T(z), n^{Ar}(z), n^{O}(z)), \quad (23)$$

$$\boldsymbol{n}(z_o) = \boldsymbol{n}_o(z_o, \beta_o), \quad (24)$$

where

$$\boldsymbol{n}(z) = \begin{bmatrix} n^{N_2}(z) \\ n^{O_2}(z) \end{bmatrix}, \quad (25)$$

$$\boldsymbol{f}(\boldsymbol{n}(z), z; \alpha, \sigma_R^i, N_R(z), T(z), n^{Ar}(z), n^{O}(z)) = \frac{1}{1 - \sigma_R^{O_2}/\sigma_R^{N_2}}\begin{bmatrix} u(z) - \sigma_R^{O_2}v(z)/\sigma_R^{N_2} \\ v(z) - u(z) \end{bmatrix}, \quad (26)$$

$$\boldsymbol{n}_o(z_o, \beta_o) = \frac{\alpha z_o^2 N_R(z_o) - \sigma_R^{Ar}n^{Ar}(z_o) - \sigma_R^{O}n^{O}(z_o)}{\sigma_R^{N_2} + \sigma_R^{O_2}\beta_o}\begin{bmatrix} 1 \\ \beta_o \end{bmatrix} \quad (27)$$

In (23) and (24) the dependence of $d\boldsymbol{n}(z)/dz$ and $\boldsymbol{n}(z_o)$ on the parameters α, σ_R^i, $N_R(z)$, $T(z)$, $n^{Ar}(z)$, $n^{O}(z)$, and β_o have been explicitly indicated for reasons that will become evident later.

Since $N_R(z)$ and $T(z)$ are measurements, $n^{N_2}(z)$ and $n^{O_2}(z)$ are in practice found by solving the modified initial value problem

$$\frac{d\boldsymbol{n}}{dz}(z) = \boldsymbol{f}(\boldsymbol{n}(z), z; \alpha, \sigma_R^i, N_R^F(z), T^F(z), n^{Ar}(z), n^{O}(z)) \quad (28)$$

$$\boldsymbol{n}(z_o^F) = \boldsymbol{n}_o(z_o^F, \beta_o^F) \quad (29)$$

The profiles $N_R^F(z)$ and $T^F(z)$ on the right-hand side of (28) are produced by filtering $N_R(z)$ and $T(z)$, respectively, using a 21 point Kaiser-Bessel filter. The derivatives $dN_R^F(z)/dz$ and $dT^F(z)/dz$ on the right-hand side of (28) are computed from $N_R^F(z)$ and $T^F(z)$, respectively, using a seven point differentator. The filtering and differentiating truncates data so that $N_R^F(z)$, $T^F(z)$, $dN_R^F(z)/dz$, and $dT^F(z)/dz$ are all valid only in a height interval 80 km $\cong z_o < z_o^F \le z \le z_f^F < z_f \cong 105$ km, where the subscripts refer to the initial and final altitudes of the retrieval. The truncation is sufficiently small such that $z_o^F \cong 80$ km and $z_f^F \cong 105$ km. Because of the truncation, a new initial value $\boldsymbol{n}_o(z_o^F, \beta_o^F)$ is used where β_o^F is the value of $n^{O_2}(z_o^F)/n^{N_2}(z_o^F)$ computed using the MSIS model.

The initial value problem of (28) and (29) is solved using a fourth-order Runge-Kutta method. To determine if the derivation of (23) and (24) is correct, and to test the accuracy of the

Runge-Kutta method used to solve (28) and (29), a test was performed using a Rayleigh photocount profile and a temperature profile based on the MSIS model. The altitudes z_o^F and z_f^F in (28) and (29) were taken to be 80 km and 105 km respectively. All of the quantities α, $N_R^F(z)$, $T^F(z)$, $dN_R^F(z)/dz$, $dT^F(z)/dz$, $n^{Ar}(z)$, $n^O(z)$, and β_o^F in (28) and (29) were computed directly from the MSIS model. The Runge-Kutta method was then used to solve (28) and (29). In this way, solutions $n^{N_2}(z)$ and $n^{O_2}(z)$ were obtained. The same two density profiles were then taken directly from the MSIS model. The agreement between the two sets of results was excellent.

4. A Method for Determining the Density of Atomic Oxygen

Suppose that the mixing ratios $n^{O_2}(z)/n^{N_2}(z)$ and $n^{Ar}(z)/n^{N_2}(z)$ are known at a height z in the upper mesosphere and lower thermosphere. For instance, suppose that the values of $n^{O_2}(z)/n^{N_2}(z)$ and $n^{Ar}(z)/n^{N_2}(z)$ are accurately predicted by the MSIS model. Then, the densities of O could be inferred at altitudes in the upper mesosphere and lower thermosphere. Let $\beta(z)$ and $\gamma(z)$ be defined such that

$$\frac{n^{O_2}(z)}{n^{N_2}(z)} = \beta(z), \tag{30}$$

$$\frac{n^{Ar}(z)}{n^{N_2}(z)} = \gamma(z) \tag{31}$$

Equations (10)-(12) and (30)-(31) were used to derive a differential equation

$$\frac{d\boldsymbol{n}}{dz}(z) = \boldsymbol{g}(\boldsymbol{n}(z), z; \alpha, \sigma_R^i, N_R(z), T(z), \beta(z), \gamma(z)), \tag{32}$$

where

$$\boldsymbol{n}(z) = [n^{N_2}(z)\ n^{O_2}(z)\ n^{Ar}(z)\ n^O(z)]^\dagger, \tag{33}$$

where the dagger symbol denotes the transpose of the row vector. Thus $n^O(z)$ can be found in the height interval 80 km $\cong z_o \le z \le z_f \cong$ 105 km by solving (32) subject to some initial condition for $\boldsymbol{n}(z)$ at $z = z_o$. A detailed study was carried out to examine the feasibility of this method for determining O densities. Because the densities of O are very small in the height interval 80 km $\cong z_o \le z \le z_f \cong$ 105 km, it was concluded that they could be reliably measured by this method only if an approximately 100-fold improvement was made in the accuracy of our lidar measurements and in the accuracy with which the parameters α, σ_R^i, $\beta(z)$, and $\gamma(z)$ can presently be determined. Hence we thought it premature to attempt to retrieve O profiles from our measurements (though the above method was successfully tested on a simulated retrieval based on the MSIS model).

5. Error Analysis of the Density Retrieval

5.1. Uncertainties in the Parameters of the Modified Initial Value Problem

The initial value problem of (28) and (29) depends on the parameters R, M^i, $g(z)$, α, σ_R^i, $N_R^F(z)$, $T^F(z)$, $n^{Ar}(z)$, $n^O(z)$, and β_o^F. The uncertainties in R, M^i, and $g(z)$ are negligible, so the dependence of (28) and (29) on these parameters has not been explicitly indicated. Table 2 gives the uncertainties of the relevant parameters. These uncertainties have been divided into two distinct categories, namely, random and systematic uncertainties. Random uncertainties in an experiment arise from fluctuations in observations which produce different results when the experiment is repeated. In contrast, systematic uncertainties produce discrepancies in results that are reproducible [*Bevington and Robinson* 1992]. In this study, the random uncertainties can be reduced by coadding, averaging, or filtering, but the systematic uncertainties are not so easily controlled.

Because (28) and (29) depend on parameters that have uncertainties, the solutions $n^{N_2}(z)$ and $n^{O_2}(z)$ to (28) and (29) must also have uncertainties $\delta n^{N_2}(z)$ and $\delta n^{O_2}(z)$, respectively; that is, the solution $\boldsymbol{n}(z)$ to (28) and (29) must have an uncertainty $\delta\boldsymbol{n}(z)$, where $\delta\boldsymbol{n}(z)$ is defined such that $\delta\boldsymbol{n}(z) = [\delta n^{N_2}(z)\ \delta n^{O_2}(z)]^\dagger$. To determine the uncertainty $\delta\boldsymbol{n}(z)$, the parameters of (28) and (29) are repeatedly perturbed in ways that reflect their uncertainties, and (28) and (29) are repeatedly solved using the resulting perturbed parameters in place of the unperturbed parameters. In this way, a sequence of perturbed solutions are generated. The sample standard deviation of this sequence is taken to be the uncertainty of the unperturbed solution to (28) and (29).

5.2. Generating the Perturbed Parameters

5.2.1. Gaussian, Poisson, and uniformly distributed random number generators. To perturb the parameters of (28) and (29), three different types of random number generators are used. As l takes on the values 1, 2, 3, ..., let $G_k^j(q, \delta q; l)$ produce random numbers that have a Gaussian distribution with a mean q and a sample standard deviation δq, $P_k^j(q; l)$ produce random numbers that have a Poisson distribution with a mean q and hence a sample standard deviation $\sqrt{q}$, and $U_k^j(q, \delta q; l)$ produce random numbers that are uniformly distributed in the interval $(q - \delta q, q + \delta q)$. Most programming languages have functions or procedures that act like Gaussian, Poisson, or uniformly distributed random number generators. The labels j and k in $G_k^j(q, \delta q; l)$, $P_k^j(q; l)$, and $U_k^j(q, \delta q; l)$ can be integers, real numbers, other literal symbols, etc. They are used to distinguish between different generators. For example, $G_1^a(q, \delta q; l)$ is not necessarily equal to $G_1^b(q, \delta q; l)$, and $P_1^a(q; l)$ is not necessarily equal to $P_{2.2}^a(q; l)$.

5.2.2. Generating perturbed values of the scalar parameters. Using Gaussian distributed random number generators, perturbed values of the parameters α, σ_R^i, and β_o^F can be generated in a straightforward way. For example, $G_1^\alpha(\alpha, \delta\alpha; l)$ produces perturbed values of α which vary as prescribed in Table 2 as l is incremented.

5.2.3. Generating perturbed values of the Rayleigh photocount and temperature profiles. Perturbed values of the profiles $N_R^F(z)$ and $T^F(z)$ are generated in a rather complicated manner described below.

1. Eighth-degree polynomials $N_R^P(z)$ and $T^P(z)$ are fitted to the noisy profiles $N_R(z)$ and $T(z)$, respectively, in the least squares sense. These fitted polynomials are taken to represent the true profiles that would have been obtained in the absence of noise.

2. Perturbed values of $N_R^P(z)$ and $T^P(z)$ are produced by the number generators $P_z^{N_R^P}(N_R^P(z); l)$, $G_z^{T^P}(T^P(z), \delta_r T(z); l)$, and $G_z^{T^P}(T^P(z), \delta_s T(z); l)$. Recall that the labels j and k in $P_k^j(q; l)$ are used to distinguish between different random number generators. For $z' \neq z$, the sequences generated by

$P_z^{N_R^P}(N_R^P(z');l)$ and $P_z^{N_R^P}(N_R^P(z);l)$ as l is incremented are completely uncorrelated even if $N_R^P(z') = N_R^P(z)$. In other words, a plot of $P_z^{N_R^P}(N_R^P(z);l)$ versus z for fixed l is a noisy version of the plot of $N_R^P(z)$ versus z. Similar comments apply to the plots of $G_z^{T^P}(T^P(z), \delta_r T(z);l)$ versus z and $G_z^{T^P}(T^P(z), \delta_s T(z);l)$ versus z.

3. The perturbed height profiles $P_z^{N_R^P}(N_R^P(z);l)$, $G_z^{T^P}(T^P(z), \delta_r T(z);l)$ and $G_z^{T^P}(T^P(z), \delta_s T(z);l)$ are filtered using the 21 point Kaiser-Bessel filter. The resulting filtered profiles are denoted by $N_R^F(z;l)$, $T_r^F(z;l)$, and $T_s^F(z;l)$ respectively.

4. Finally, (28) and (29) are again solved using the resulting filtered profiles $N_R^F(z;l)$, $T_r^F(z;l)$, and $T_s^F(z;l)$ in place of $N_R^F(z)$ and $T^F(z)$.

By generating perturbed values of the profiles $N_R^F(z)$ and $T^F(z)$ in the way described above, we estimate the contribution of the uncertainties in $N_R(z)$ and $T(z)$ to the overall uncertainty $\delta \boldsymbol{n}(z)$ in the solution $\boldsymbol{n}(z)$ to (28) and (29). The method described above may seem convoluted. Nevertheless, it properly takes into account the effect of filtering $N_R(z)$ and $T(z)$ before solving (28) and (29).

5.2.4. Generating perturbed values of the argon and atomic oxygen density profiles. Equations (28) and (29) are solved using the profiles $n^{Ar}(z)$ and $n^O(z)$. These profiles are not obtained by filtering; instead, they are taken directly from the MSIS model. Consequently, the perturbed values of $n^{Ar}(z)$ and $n^O(z)$ cannot be generated in the same way as the perturbed values of $N_R^F(z)$ and $T^F(z)$. Because the right-hand side of (28) depends on the derivatives $dn^{Ar}(z)/dz$ and $dn^O(z)/dz$, the density profiles produced by perturbing $n^{Ar}(z)$ and $n^O(z)$ are not noisy data series with sharply discontinuous first derivatives. Such density profiles are not physically realistic in the sense that no geophysical variability is present. In addition, all sorts of unpre-

Table 2. Uncertainties in the Parameters α, σ_R^i, $N_R(z)$, $T(z)$, $n^{Ar}(z)$, $n^O(z)$ and β_o^F.

Parameter	Source of Uncertainty	Type	Symbol	Value	Interpretation
$N_R(z)$	Photon noise.	random	$\delta_r N_R(z) = \sqrt{N_R(z)}$	depends on coadding	If the parameter was repeatedly measured, the sequence of measurements would be Poisson distributed and would have a mean equal to the estimated value of the parameter and a sample standard deviation equal to the parameter's uncertainty.
$T(z)$	Photon noise.	random	$\delta_r T(z)$	depends on coadding	If the parameter was repeatedly measured, the sequence of measurements would be Gaussian distributed and would have a mean equal to the estimated value of the parameter and a sample standard deviation equal to the parameter's uncertainty.
α			$\delta_s \alpha$	5%	
$n^{Ar}(z)$	Inaccuracy of the MSIS model.	systematic	$\delta_s n^{Ar}(z)$	50%	
$n^O(z)$			$\delta_s n^O(z)$	50%	
β_o^F			$\delta_s \beta_o^F$	10%	
σ_R^i, $i = N_2, O_2, Ar$	Errors in measurements of the cross sections [e.g., *Rudder and Bach*, 1968].	systematic	$\delta_s \sigma_R^i$, $i = N_2, O_2, Ar$	5%	Let j be the estimated value of the parameter being considered, and let $\delta_s j$ be the estimated value of its uncertainty. If the parameter was repeatedly measured, the sequence of measurements would be Gaussian distributed and would have a mean j and a sample standard deviation $\delta_s j$.
σ_R^O	Approximations made in the theoretical calculation presented by *Stergis* [1966].	systematic	$\delta_s \sigma_R^O$	50%	
$T(z)$	Instrumental errors: laser frequency and rms line width. Geophysical errors: sodium radial velocity and sodium density variations. See *Argall et al.* [2000] for a detailed discussion.	systematic	$\delta_s T(z)$	1.5 K	

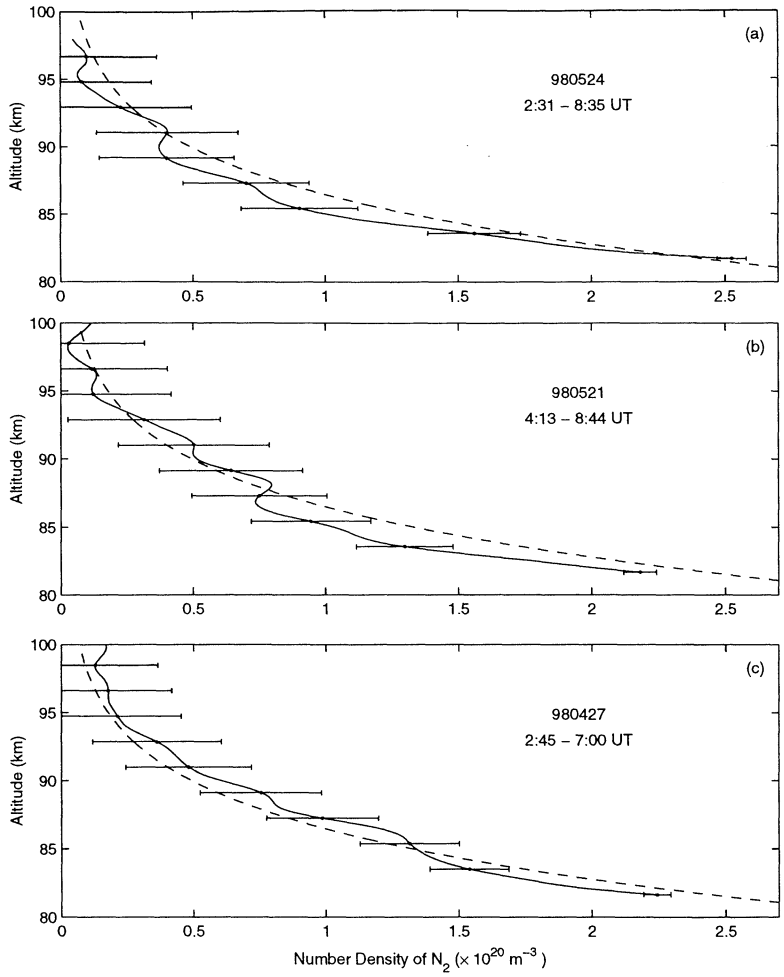

Figure 1. N_2 number density as a function of height (solid line) retrieved from Purple Crow Lidar measurements on three nights. The horizontal error bars indicate the uncertainties in these profiles due to the random uncertainties described in Table 2. The dashed curves are the number densities of N_2 predicted by the MSIS model. For each night, the integration time is shown in the figure.

dictable problems would arise when (28) and (29) were solved numerically using the perturbed profiles in place of $n^{\mathrm{Ar}}(z)$ and $n^{\mathrm{O}}(z)$. To produce continuous perturbed functions, a special number generator $D^j(q(z), \delta q(z), z; l)$ is used whose variations have a magnitude based on the known variability of the species (see Table 2). The form of this number generator is

$$D^j(q(z), \delta q(z), z; l) = q(z) + \delta q(z) \times 1.2290 \times \tag{34}$$

$$\left\{ G_1^j(0, 1; l) \sin\left[\frac{\pi(z - z_o)}{z_f - z_o} + U_1^j(0, \pi; l)\right] \right.$$

$$+ G_2^j(0, 1/2; l) \sin\left[\frac{4\pi(z - z_o)}{z_f - z_o} + U_2^j(0, \pi; l)\right]$$

$$+ G_3^j(0, 1/4; l) \sin\left[\frac{16\pi(z - z_o)}{z_f - z_o} + U_3^j(0, \pi; l)\right]$$

$$\left. + G_4^j(0, 1/8; l) \sin\left[\frac{32\pi(z - z_o)}{z_f - z_o} + U_4^j(0, \pi; l)\right] \right\}$$

The form of (34) was decided upon by experimentation on a computer. For any given l, the plot of $D^j(q(z), \delta q(z), z; l)$ versus z is a superposition of two height profiles. The first is the initial density profile $q(z)$. The second is a wavelike perturbation that is the sum of four sine waves chosen such that the resulting superposition $D^j(q(z), \delta q(z), z; l)$ versus z would be a realistic density profile. The detailed spatial structure of the wavelike perturbation depends on the amplitudes and phases of the sine waves. As l is incremented, the amplitudes and phases of the sine waves take on sequences of values which are, respectively, Gaussian and uniformly distributed. Thus the spatial structure of the wavelike perturbation varies as l varies. Sometimes the wavelike perturbation is small; sometimes its large. Sometimes it oscillates rapidly over a given height interval; sometimes it steadily increases or decreases. The numerical coefficient 1.2290 was specially chosen so that the sequence generated by $D^j(q(z), \delta q(z), z; l)$ as l is incremented is for all z approximately Gaussian distributed with a mean $q(z)$ and a sample standard deviation $\delta q(z)$.

5.3. Uncertainties in the Retrieved Densities

To find the uncertainty $\delta \boldsymbol{n}(z)$ in the solution $\boldsymbol{n}(z)$ of (28) and (29) due to the random uncertainties in the parameters of (28) and (29), the following initial value problems are solved:

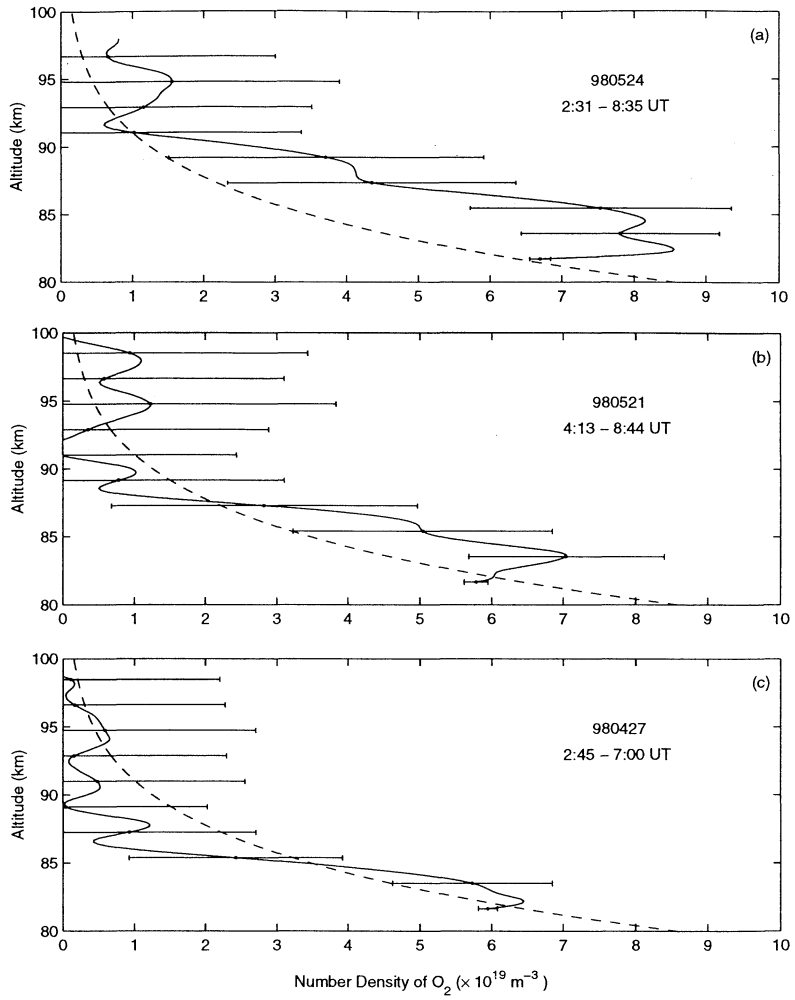

Figure 2. O_2 number density as a function of height (solid line) retrieved from Purple Crow Lidar measurements on the same nights as shown in Figure 1. The horizontal error bars indicate the uncertainties in these profiles due to the random uncertainties described in Table 2. The dashed curves are the number densities of O_2 predicted by the MSIS model. For each night, the integration time is shown on the figure.

$$\frac{d\boldsymbol{n}}{dz}(z;l) = \boldsymbol{f}(\boldsymbol{n}(z;l), z; \alpha, \sigma_R^i, N_R^F(z;l), T_r^F(z;l), n^{Ar}(z), n^O(z)), \quad (35)$$

$$\boldsymbol{n}(z_o^F;l) = \boldsymbol{n}_o(z_o^F, \beta_o^F), \quad (36)$$

for $l = 1, 2, 3, \ldots, l_f$. Compare (35) and (36) to (28) and (29). Only the parameters $N_R(z)$ and $T(z)$ have random uncertainties. Therefore only the perturbed values of $N_R^F(z)$ and $T^F(z)$ appear in (35) and (36). The derivatives $dN_R^F(z;l)/dz$ and $dT_r^F(z;l)/dz$ on the right-hand side of (35) are computed from $N_R^F(z;l)$ and $T_r^F(z;l)$, respectively, again using a seven point differentator. Solving (35) and (36) for $l = 1, 2, 3, \ldots, l_f$ generates a sequence of solutions $\boldsymbol{n}(z;1)$, $\boldsymbol{n}(z;2)$, ..., $\boldsymbol{n}(z;l_f)$. Let $\bar{\boldsymbol{n}}(z)$ be defined such that

$$\bar{\boldsymbol{n}}(z) = \lim_{l_f \to \infty} \frac{1}{l_f} \sum_{l=1}^{l_f} \boldsymbol{n}(z;l) \quad (37)$$

Then, the uncertainty $\delta\boldsymbol{n}(z)$ in the solution $\boldsymbol{n}(z)$ of (28) and (29) is defined to be

$$\delta\boldsymbol{n}(z) = \lim_{l_f \to \infty} \sqrt{\frac{1}{l_f - 1} \sum_{l=1}^{l_f} [\boldsymbol{n}(z;l) - \bar{\boldsymbol{n}}(z)]^2} \quad (38)$$

The quantities $\bar{\boldsymbol{n}}(z)$ and $\delta\boldsymbol{n}(z)$ are the mean and sample standard deviation, respectively, of the sequence of solutions $\boldsymbol{n}(z;1)$, $\boldsymbol{n}(z;2)$, ..., $\boldsymbol{n}(z;l_f)$ in the limit $l_f \to \infty$. In practice, the limits in (37) and (38) are found to converge rapidly. Consequently, the following approximations can be made with very little loss of accuracy:

$$\bar{\boldsymbol{n}}(z) = \frac{1}{l_f} \sum_{l=1}^{l_f} \boldsymbol{n}(z;l), \quad (39)$$

$$\delta\boldsymbol{n}(z) = \sqrt{\frac{1}{l_f - 1} \sum_{l=1}^{l_f} [\boldsymbol{n}(z;l) - \bar{\boldsymbol{n}}(z)]^2}, \quad (40)$$

where $l_f = 250$. To find the uncertainty $\delta\boldsymbol{n}(z)$ in the solution $\boldsymbol{n}(z)$ of (28) and (29) due to the systematic uncertainties in the

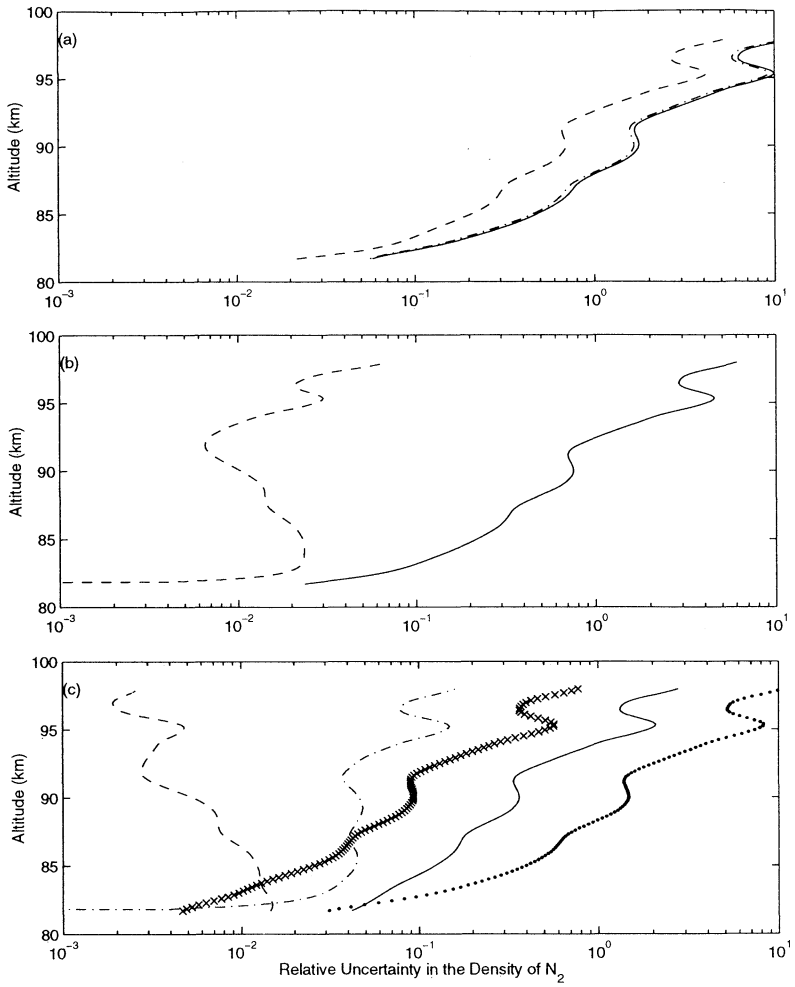

Figure 3. Relative uncertainty $\delta n^{N_2}(z)/n^{N_2}(z)$ for the retrieval shown on May 24, 1998 (Figure 1a). (a) Plots of $\delta n^{N_2}(z)/n^{N_2}(z)$ due to the sum of the random uncertainties (solid line), and the sum of the systematic uncertainties (dashed line) as described in Table 2. (b) The solid and dashed lines are the uncertainties in $\delta n^{N_2}(z)/n^{N_2}(z)$ due to $\delta_r N_R(z)$ and $\delta_r T(z)$ respectively. (c) The uncertainty of $\delta n^{N_2}(z)/n^{N_2}(z)$ due to $\delta_s \alpha$ (solid line), $\delta_s \beta_o^F$ (dashed line), $\delta_s T(z)$ (dotted-dashed line), $\delta_s \sigma_R^{N_2}$ and $\delta_s \sigma_R^{O_2}$ (dotted line), and $\delta_s \sigma_R^{Ar}$, $\delta_s \sigma_R^{O}$, $\delta_s n^{Ar}(z)$, and $\delta_s n^{O}(z)$ (crossed line).

parameters of (28) and (29), the following initial value problems are solved in place of (35) and (36):

$$\frac{d\boldsymbol{n}}{dz}(z;l) = f\Big(\boldsymbol{n}(z;l), z; G_1^{\alpha}(\alpha, \delta\alpha; l), G_1^{\sigma_R^i}(\sigma_R^i, \delta\sigma_R^i; l), \quad (41)$$

$$N_R^F(z), T_s^F(z;l), D^{n^{Ar}}(n^{Ar}(z), \delta n^{Ar}(z), z; l),$$

$$D^{n^{O}}(n^{O}(z), \delta n^{O}(z), z; l)\Big)$$

$$\boldsymbol{n}(z_o^F; l) = \boldsymbol{n}_o\Big(z_o^F, G_1^{\beta_o^F}(\beta_o^F, \delta\beta_o^F; l)\Big), \quad (42)$$

for $l = 1, 2, 3, \ldots, l_f = 250$. The uncertainty $\delta\boldsymbol{n}(z)$ in the solution $\boldsymbol{n}(z)$ due to an uncertainty in only one of the parameters can be estimated in a similar way.

6. N_2 and O_2 Density Retrievals Using Purple Crow Lidar Measurements

The method and error analysis described in the previous sections was applied to three nights of simultaneous measurements using the Purple Crow Lidar Rayleigh-scatter and sodium-resonance-fluorescence systems. Representative photocount profiles of the quality used for input to the composition retrieval are shown by *Sica et al.* [1995]. The sodium-resonance-fluorescence temperature profiles used are shown by *Argall et al.* [2000].

The N_2 density profiles retrieved on the three nights are shown in Figure 1. The agreement between the retrieved N_2 profiles and the MSIS model for the same geophysical conditions is encouraging. On May 24 and 21, 1998 (Figures 1a and 1b), the N_2 densities retrieved from the lidar measurements are about 15% less than the model below 90 km and about the same above this height. On April 27, 1998 (Figure 1c), the N_2 densities below 85 km are less than the MSIS values, then consistently about 20% greater above this height.

The retrieved O_2 density profiles shown in Figure 2 show larger discrepancies with the MSIS model, even allowing for the larger random error of these estimates. On May 24, 1998 (Figure 2a), the O_2 is considerably higher (by a factor of 1.5) than the MSIS model. On May 21 and April 24 (Figures 2b and 2c) the O_2 densities are quite low above 85 km with little altitude variation and magnitudes of about 5 x 10^{18} m^{-3}. Below this height the O_2 density is greater than that given by the MSIS model.

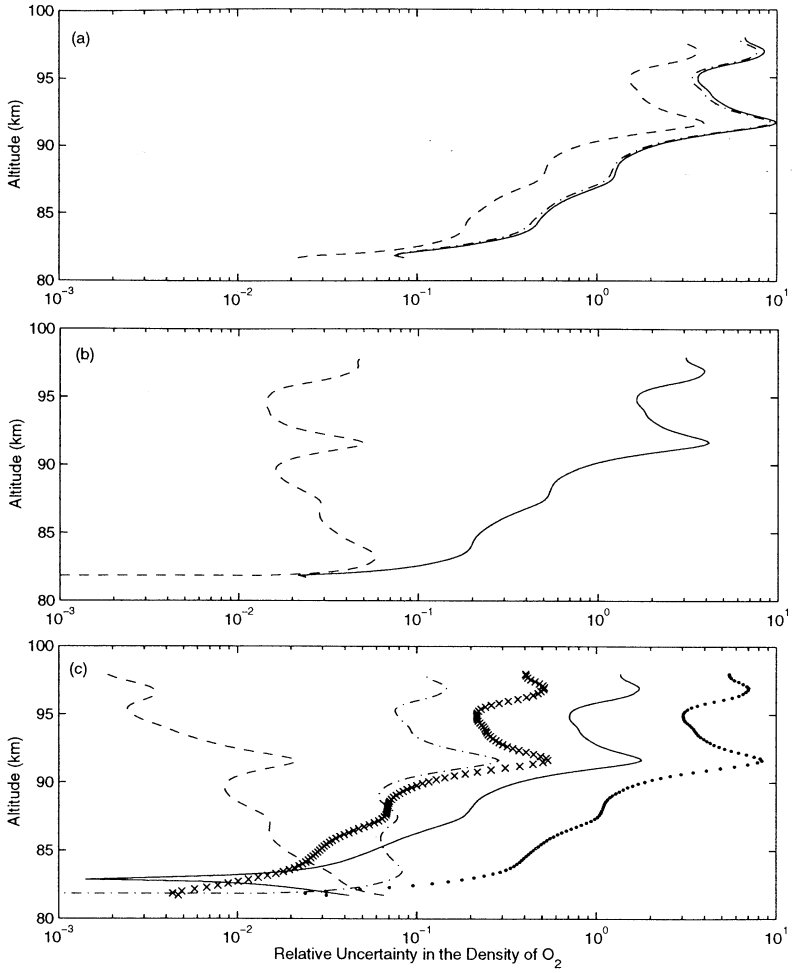

Figure 4. Relative uncertainty of $\delta n^{O_2}(z)/n^{O_2}(z)$ in the same format as Figure 3 for May 24, 1998 (Figure 2a). Solid lines are the mean molecular mass computed using the measurements shown in Figures 1 and 2. The dashed lines are obtained from the MSIS model. The horizontal error bars indicate the uncertainties due to the random uncertainties described in Table 2.

Figures 3 and 4 show a breakdown of the uncertainties associated with the density retrievals. The random errors (Figures 3b and 4b) are almost entirely due to photon noise statistics of the Rayleigh photocount profiles. However, as Figures 3a and 4a show, the random errors are less than half of the systematic errors. These systematic errors are almost entirely due to uncertainties in the major constituent cross sections and, to a lesser degree, to the choice of normalization of the density profiles. The assumption of Ar and O density, the associated cross sections of these constituents, and the absolute errors in the sodium temperature determinations are 10 to 100 times smaller than the other systematic errors. Essentially negligible is the error due to the choice of a seed value for the major constituent composition ratio β_0.

7. Discussion

Despite N_2 and O_2 comprising more than 99% of the atmospheric mass in the upper mesosphere and lower thermosphere, relatively few measurements of these species are available, and the references we have been able to find are more than 15 years old. For instance, Philbrick and colleagues [*Philbrick et al.*, 1973, 1974, 1978] have found variations in the Ar to N_2 ratios of 30% at midlatitudes. They also measured rapid changes in the O_2 mixing ratio relative to the surface above 90 km. During one of their flights they saw large density variations attributed to gravity waves. *Krankowsky et al.* [1979] measured O_2 density changes of factors of 2 to 5 times in the 85 to 98 km altitude region during a series of flights during the midlatitude winter. *Offermann et al.* [1981] reported mixing ratios of O_2 to N_2 in the upper mesosphere and lower thermosphere which were smaller than their sea level value by as much as 40%, though their results were relatively constant with altitude. To our knowledge, no climatology of these rocket measurements exist, just isolated flights and campaigns. Our results are consistent with the previous studies and open the possibility of climatologies of the major constituent densities to be determined.

Our results have implications for the retrieval of temperature from Rayleigh-scatter (or in general, any) density measurements. The temperature profiles determined by the Rayleigh technique depend on both the mean molecular mass and the Rayleigh backscatter cross section of air. Our initial results suggest that the mean molecular mass is not typically constant with height, nor equal to the sea level value, in the upper mesosphere and lower thermosphere (Figure 5). On May 21, 1998 (Figure 5b), the mean molecular mass is about the same as the MSIS model, while on May 24 (Figure 5a), it is a few percent larger, and on April 27 (Figure 5c), it is a few percent smaller. Accounting for these changes in mean molecular mass will change the retrieved Rayleigh-scatter temperatures compared to temperatures determined using a constant

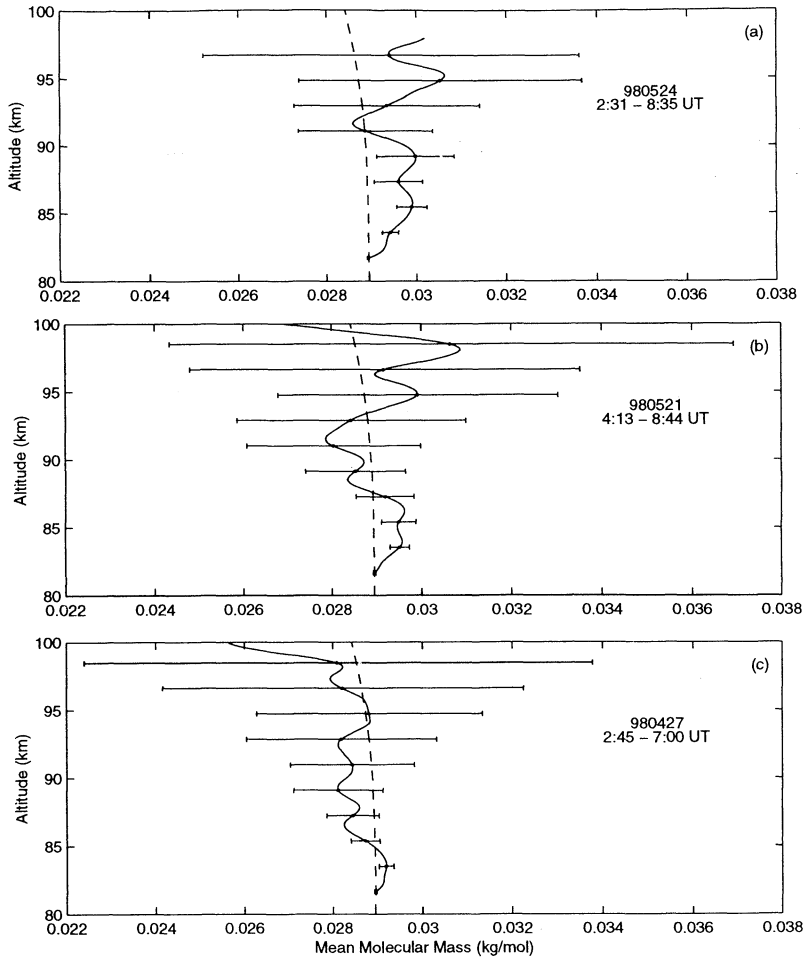

Figure 5. Solid lines are the mean molecular mass computed using the measurements shown in Figures 1 and 2. The dashed lines are obtained from the MSIS model. The horizontal error bars indicate the uncertainties due to the random uncertainties described in Table 2.

mean molecular mass. In most cases, below 100 km, these temperature differences are expected to be small compared to measurement errors, but we anticipate performing a more through study of these differences when sufficient coincident Purple Crow Rayleigh and sodium lidar measurement sets become available.

The Rayleigh-scatter-derived density and temperature profiles are quite sensitive to the choice of Rayleigh backscatter cross section, which our results show varies with altitude in the upper mesosphere and lower thermosphere. Choice of cross section can cause differences in temperature of several degrees (or more), as shown in the temperature profiles of *Argall et al.* [2000]. At timescales of a few hours or less, composition variations may cause significant differences in Rayleigh-scatter temperature determinations compared to other methods. On the other hand, it may be incorrect to attribute the entire difference between our Rayleigh-scatter and sodium-resonance-fluorescence temperature measurements to composition as we have assumed in this pilot study in part because the extent of uncertainty of the sodium temperatures due to geophysical variability may have been underestimated (Table 2).

8. Summary and Conclusions

Two new techniques have been presented to infer density profiles in the middle atmosphere, one for N_2 and O_2, the other for N_2, O_2, and O. The initial value problem for N_2 and O_2 has been applied to lidar measurements in the upper mesosphere and lower thermosphere and has produced results that are consistent with previous measurements and the MSIS model. The initial value problem for N_2, O_2, and O was found to work successfully on lidar measurements simulated using the MSIS model but cannot be applied to current lidar measurements until significant improvements to the quality of the measurements are realized. Some specific results of this study include the following:

1. Initial value problems have been formulated which allow the calculation of N_2 and O_2 densities in the middle atmosphere. The requirements for the calculation are Rayleigh-scatter photocount measurements and a determination of the temperature profile independent of the Rayleigh-scatter measurement.
2. A detailed error analysis has been given allowing the effects of both random and systematic errors to be determined. The most significant random error is in the Rayleigh photocount profiles. The most significant systematic error is in our knowledge of the Rayleigh backscatter cross sections of N_2 and O_2.
3. N_2 and O_2 density profiles have been determined from Purple Crow Lidar measurements that appear reasonable when compared against in situ measurements by rockets and the MSIS model.

The overall errors in this pilot study are quite large. We look forward to improved measurements of the relevant cross sections

necessary to decrease the systematic errors. We plan to continue our measurements of N_2 and O_2 densities, as well as evaluate the possible effects of these compositional variations on temperature retrievals using the Rayleigh-scatter technique. We also look forward to improvements in the power-aperture product of future lidar systems, both to expand these studies to other locations and to decrease the random errors of the density determinations.

Acknowledgments. We would like to thank O. Vassiliev, Randy S. Kissack and Albert Russell at the University of Western Ontario for helpful discussions, and the National Science and Engineering Research Council of Canada for support of this research. We would also like to thank the reviewers for their comments, which have improved the manuscript.

References

Argall, P. S., O. N. Vassiliev, R. J. Sica, and M. M. Mwangi, Lidar measurements taken with a large-aperture liquid mirror, 2, Sodium-resonance-fluorescence system, *Appl. Opt., 39*, 2393-2400, 2000.

Bevington, P. R., and D. K. Robinson, *Data Reduction and Error Analysis for the Physical Sciences*, 2nd ed., pp. 3-6, McGraw-Hill, New York, 1992.

Cole, A. E., and A. J. Kantor, Interlevel correlations of temperature and density, surface to 60 km, *AFGL TR-80-0163, ADA090515*, Air Force Geophys. Lab., Bedford, Mass., 1980.

Fricke, K. H., and U. von Zahn, Mesopause temperatures derived from probing the hyperfine structure of the D_2 resonance line of sodium lidar, *J. Atmos. Sol. Terr. Phys., 47*, 499-512, 1985.

Gardner, C. S., D. C. Senft, T. J. Beatty, R. E. Bills, and C. A. Hostetler, Rayleigh and sodium lidar techniques for measuring middle atmospheric density, temperature, and wind perturbations and their spectra, in *World Ionosphere/Thermosphere Study Handbook*, vol. 2, chap. 6, edited by C. H. Liu, ICSU Sci. Comm. on Sol. Terr. Phys., Urbana, Ill., 1989.

Gibson, A., L. Thomas, and S. Bhattachacharyya, Laser observation of ground-state hyperfine structure of sodium and of temperatures in the upper mesosphere, *Nature, 281*, 131-132, 1979.

Hauchecorne, A., and M.-L. Chanin, Density and temperature profiles obtained by LIDAR between 35 and 70 km, *Geophys. Res. Lett., 7*, 565-568, 1980.

Hedin, A. E., MSIS-86 thermospheric model, *J. Geophys. Res., 92*, 4649-4662, 1987.

Krankowsky, D., F. Arnold, V. H. Friedrich, and D. Offermann, Neutral atmospheric composition measurements during the Western European Winter Anomaly Campaign 1975/76, *J. Atmos. Sol. Terr. Phys., 41*, 1085-1090, 1979.

Measures, R. M., *Laser Remote Sensing: Fundamentals and Applications*, pp. 38-47, John Wiley, New York, 1984.

Offermann, D., V. Friedrich, P. Ross, and U. von Zahn, Neutral gas composition measurements between 80 and 120 km, *Planet Space Sci., 29*, 747-764, 1981.

Philbrick, C. R., G. A. Faucher, and E. Trzcinsky, Rocket measurements of mesospheric and lower thermospheric composition, in *Space Research*, vol. 13, pp. 255-260, Academic, San Diego, Calif., 1973.

Philbrick, C. R., D. Golomb, S. P. Zimmerman, T. J. Keneshea, M. MacLeod, R. E. Good, B. S. Dandekar, and B. W. Reinisch, The Aladdin II Experiment, part II, Composition, in *Space Research*, vol. 14, pp 89-95, Academic, San Diego, Calif., 1974.

Philbrick, C. R., G. Faucher, and P. Bench, Composition of the mid-latitude winter mesosphere and lower thermosphere, in *Space Research*, vol. 18, pp. 139-142, Pergamon, New York, 1978.

Rudder, R. D., and D. R. Bach, Rayleigh scattering of ruby-laser light by neutral gases, *J. Opt. Soc. Am., 58*, 1260-1266, 1968.

She, C. Y., J. R Yu, H. Latifi, and R. E. Bills, High-spectral-resolution fluorescence light detection and ranging for mesospheric sodium temperature measurements, *Appl. Opt., 31*, 2095-2106, 1992.

Sica, R. J., S. Sargoytchev, P. S. Argall, E. F. Borra, L. Girard, C. T. Sparrow, and S. Flatt, Lidar measurements taken with a large-aperture liquid mirror, 1, Rayleigh-scatter system, *Appl. Opt., 34*, 6925-6936, 1995.

Stergis, C. G., Rayleigh scattering in the upper atmosphere, *J. Atmos. Sci., 28*, 273-284, 1966.

Trinks, H., D. Offermann, U. von Zahn, and C. Steinhauer, Neutral composition measurements between 90 and 220 km altitude by rocket-borne mass spectrometer, *J. Geophys. Res., 83*, 2169-2176, 1978.

P. S. Argall, M. M. Mwangi, and R. J. Sica, Department of Physics and Astronomy, The University of Western Ontario, London, ON, N6A 3K7, Canada. (sica@uwo.ca)

(Received August 25, 1999; revised September 21, 2000; accepted October 2, 2000.)